Plasmonics
https://doi.org/10.1007/s11468-024-02522-y

RESEARCH

Compact Three-Channel Photonic Crystal Fiber Sensor Based on Surface Plasmon Resonance

Tianli Huo[1] · Xili Jing[1] · Zhiyong Yin[1] · Tianci Gao[1] · Mingshi Song[1]

Received: 5 August 2024 / Accepted: 28 August 2024

Abstract

In order to improve the integration of fiber optic sensors, this paper designs a dual-core three-channel photonic crystal fiber (PCF) optic sensor that can simultaneously measure the refractive index of a liquid, its temperature, and the ambient magnetic field. Based on the PCF as well as SPR principles, the sensor has two D-planes, one coated with PDMS as well as a gold film for detecting temperature and the other coated with a gold film for detecting refractive index and coated with a gold film over the air holes on the side of the core where the refractive index is measured and a magnetic fluid injected into the air holes to detect the magnetic field. The results show a maximum sensitivity of 20,000 nm/RIU for refractive index, a linear sensitivity of 116 pm/Oe for magnetic field, and 5300 pm/°C for temperature when the sample's refractive index is between 1.36 and 1.42, the temperature is between 0 °C and 50 °C, and the magnetic field is between 20 and 550 Oe. The sensitivity matrix of temperature versus refractive index is also given. The sensor is compact and simple to prepare, providing a new solution for miniaturization and integration of multifunctional photonic devices.

Keywords Photonic crystal fiber · Surface plasmon resonance · Sensitivity matrix · Magnetic field · Temperature · Refractive index

Introduction

Photonic crystal fiber (PCF), with their periodically aligned pore structure, is an excellent platform for developing sensors with many sensing advantages. Recently, researchers have combined the surface plasmon resonance (SPR) effect with PCF sensing technology to construct PCF sensors that can excite the SPR effect. This type of sensor has good sensing characteristics, which makes it suitable for sensor development [1]. SPR technology is based on the principle of total reflection. When the incident light on the surface of the fiber undergoes total reflection, part of the light will return to the fiber. The other part will propagate along the surface of the fiber in the form of a swift wave, which is interfered with by the photons and undergoes a collective oscillation to form a plasma wave, and the resonance of the surface plasma wave (SPW) with the evanescent wave occurs under a certain incident angle and wavelength to produce the SPR effect, which results in a corresponding Resonance Absorption Peak [1]. At present, SPR technology has been used in the fields of biomonitoring analysis [2–4]. PCF sensors based on the SPR effect are characterized by high sensitivity and flexible design [5, 6].

The optical phenomenon of SPR allows it to track the interactions between biomolecules in their natural state in real-time. In 2006, Hassani et al. designed a PCF based SPR sensor by combining SPR sensing with PCF for the first time [7]. This sensor has a stable structure and good sensing characteristics. However, fabricating is more difficult because its metal film and measurement channels are located in the air holes. In 2012, Ming Tian et al. proposed a D-type PCF [8]. In this structure, a meta film and a liquid are applied to the exterior of the cladding, making it easy to prepare. The above sensors can only measure one parameter, and the study of multi-parameter measurement is conducive to improving optical fiber integration. In 2021, Xiao et al. designed a PCF-SPR sensor that can perform simultaneous three-parameter measurements. The air holes

✉ Xili Jing
sljingxl@ysu.edu.cn

[1] State Key Laboratory of Metastable Materials Science & Technology and Key Laboratory for Microstructural Material Physics of Hebei Province, School of Science, Yanshan University, Qinhuangdao 066004, People's Republic of China

Published online: 09 September 2024

next to the fiber core are filled with temperature-sensitive materials and magnetic fluids, respectively, and graphene and metal films are coated on the side-throw surface of the fiber, enabling simultaneous measurement of temperature, refractive index, and magnetic field [9]. In 2022, Yin et al. designed a D-type dual-core PCF-SPR sensor. The upper throw surface is coated with temperature-sensitive material and a metal film for temperature measurement, and the lower throw surface is coated with a metal film for refractive index measurement [10]. The reported SPR-PCF sensors achieve multifunctional detection but still have the disadvantages of complex preparation and low integration and do not meet the trend of device miniaturization and integration.

This paper proposes a three-parameter dual-core PCF-SPR sensor based on the above research background. Temperature and refractive index measurements are realized by applying a metal film and temperature-sensitive material to the upper polished surface and a gold film to the lower polished surface. Air holes next to the refractive index channel cores are filled with magnetic fluid for magnetic field measurements. This makes the three-parameter sensor easier to fabricate. The detection ranges chosen for this study were temperature 0–50 °C, refractive index 1.36–1.42, and magnetic field strength 20–550 Oe. The results showed that the refractive index showed a maximum sensitivity of 20,000 nm/RIU, the linear sensitivity for temperature was 5.3 nm/°C, and the linear sensitivity for the magnetic field was 116 pm/Oe.

Theoretical Foundations and Sensing Structures

The cross-section of the sensor is shown in Fig. 1, from which it can be seen that the two sides are polished to different depths, with the upper polished depth being d_1 and the lower polished depth being d_2. The radius of the air holes is r_1, the radius of the magnetic field channel is r_2, and the spacing between the nearest neighboring air holes is c.

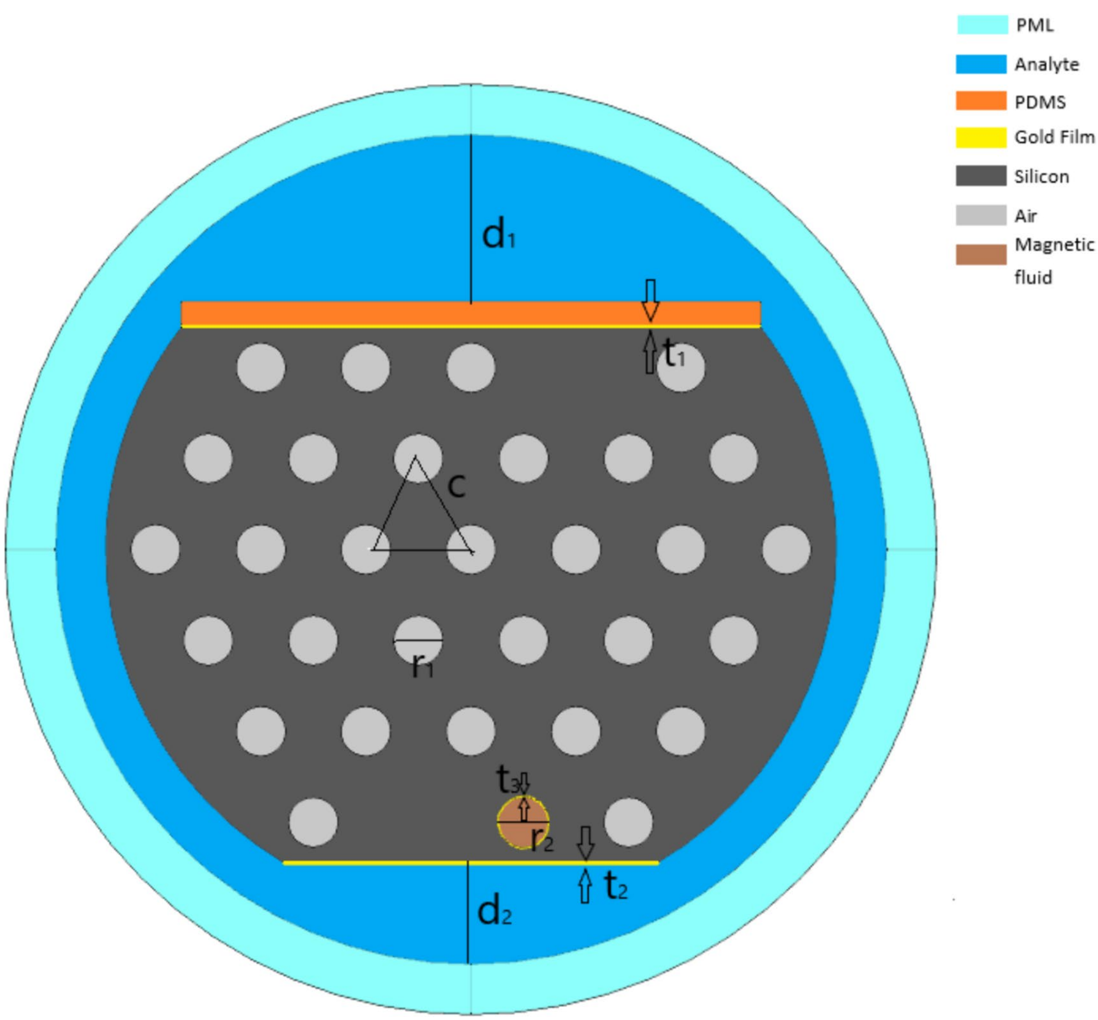

Fig. 1 Cross-section of a multi-parameter PCF

Polydimethylsiloxane (PDMS) was coated immediately adjacent to the gold film for temperature measurements. A layer of gold film with a thickness of t_2 on the lower polished surface is coated with gold for detecting the RI of the liquid, and one end of the fiber core of the lower polished surface is filled with a magnetic fluid. A gold film of thickness t_2 was coated on the lower polished surface to detect the RI of the fluid, and the air holes at one end of the fiber core on the lower polished surface were filled with magnetic fluid. The air holes were coated with a gold film to detect the magnetic field. The PDMS will be easily connected to other materials after heating. Based on the properties of PDMS as well as Si, temperature measurements can be realized [11]. Selection of Fe_3O_4 as a magnetic fluid to enable the detection of magnetic fields [12].

The following process can prepare the sensor: first, PCF preforms are obtained by ultrasonic drilling [11, 12], sol-gel [13], beam stacking [14], or extrusion [15, 16]. After that, it is processed into PCF semi-finished products [17]. Double-sided polished photonic crystal fiber can be obtained by polishing [18, 19]. Then, a gold film is applied to the two polishing planes and the surface of the air holes at one end of the fiber core (2) by magnetron sputtering. [20, 21]. Then, PDMS [22] is applied to the gold film on the upper surface. Finally, Fe_3O_4 was injected into the air holes coated with gold film using a micro syringe and plasticized. At this point, the fabrication of the sensor designed in this paper is complete, as shown in Fig. 2.

Silicon dioxide is commonly used as a material for making optical fiber, and the equation for calculating its material dispersion is as follows [23]:

$$n^2(\lambda) = 1 + \sum_{i=1}^{3} \frac{a_i\lambda^2}{\lambda^2 - b_i^2} \tag{1}$$

The dielectric constant of the gold film can be expressed in terms of the Lorentz-Drude model as follows [24]:

$$\varepsilon_r(\omega) = 1 - \frac{\Omega_p^2}{\omega\left(\omega - i\tau_0\right)} + \sum_{j=1}^{k} \frac{f_j\omega_p^2}{\left(\omega_j^2 - \omega^2\right) + i\omega\tau_j} \tag{2}$$

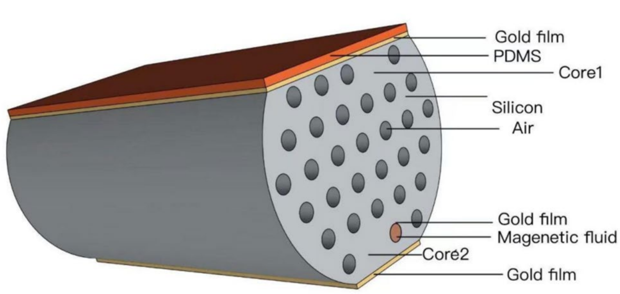

Fig. 2 Three-dimensional modeling of the PCF-SPR sensor

We can also use expressions to characterize the refractive index of the PDMS used for detecting temperature as a function of temperature [25].

$$n_{PDMS} = -4.5 \times 10^{-4} \cdot T + 1.4176 \tag{3}$$

A magnetofluid is a colloidal solution. The Langevin function expresses its dependence on temperature and magnetic field strength [26–29]. The magnetic fluid used in this simulation is $Fe_3\,O_4$. The following expression can represent its material detection expression [30].

$$n_{MF} = 1.3592 - 2.4 \times 10^{-4} \cdot T + 4.98 \times 10^{-5} \cdot H \tag{4}$$

Sensitivity is an essential index for evaluating the performance of photonic crystal fiber optic sensors, and it can be represented by the following expression [31].

$$S(\lambda) = \frac{\Delta\lambda_{\text{peak}}}{\Delta n_s}\left(\frac{\text{nm}}{\text{RIU}}\right) \tag{5}$$

The full width at half maxima (FWHM) of the resonance peak affects the sensor's resolution, and too much sensor sensitivity leads to too much FWMH, which results in lower sensor resolution [32]. For this, we choose the quality factor figure of merit (FOM) to judge the transmission characteristics [10]:

$$\text{FOM} = \frac{S(\lambda)}{\text{FWHM}} \tag{6}$$

According to the above formula, the material's refractive index changes when the magnetic field and temperature change, leading to a shift in the resonance wavelength. By observing the shift, we can calculate its sensitivity. The expression for calculating the sensitivity of the two is as follows [10]:

$$K_{ch}(T) = \Delta\lambda_{ch}/\Delta T K_{ch}(H) = \Delta\lambda_{ch}/\Delta H \tag{7}$$

We can derive the sensitivity matrices for the temperature and magnetic field channels using the following matrices:

$$\begin{pmatrix} \Delta\lambda_1 \\ \Delta\lambda_2 \end{pmatrix} = \begin{pmatrix} \frac{\lambda_{1T}}{\Delta T} & \frac{\lambda_{1H}}{\Delta H} \\ \frac{\lambda_{2T}}{\Delta T} & \frac{\lambda_{2H}}{\Delta H} \end{pmatrix} \begin{pmatrix} \Delta T \\ \Delta B \end{pmatrix} = \begin{pmatrix} K_{ch1}(T)\, K_{ch1}(H) \\ K_{ch2}(T)\, K_{ch2}(H) \end{pmatrix} \begin{pmatrix} \Delta T \\ \Delta H \end{pmatrix} \tag{8}$$

where $\Delta\lambda_{ij}$ denotes the shift of the resonance wavelengths of the temperature and magnetic field channels for temperature or magnetic field changes, ΔTand ΔH denote the changes in temperature and magnetic field, respectively, and $K_{chi(J)}$ denotes the sensitivity of the two channels to changes in temperature and magnetic field.

We can get the temperature and magnetic field sensitivity matrices by solving the inverse matrix of the above matrices [10]:

$$\begin{pmatrix} \Delta T \\ \Delta H \end{pmatrix} = \begin{pmatrix} K_{ch1}(T) & K_{ch1}(H) \\ K_{ch2}(T) & K_{ch2}(H) \end{pmatrix}^{-1} \begin{pmatrix} \Delta\lambda_1 \\ \Delta\lambda_2 \end{pmatrix} \tag{9}$$

In this simulation, we use the finite element method in Comsol to perform the analysis. The perfectly matched layer (PML) first absorbs the radiant energy of other light and allows for a stable transmission of energy in the core.

Figure 3 shows the electric field distribution. For the parameters, we chose the radius of the air holes as $r_1 = 1.5$ um, the radius of the air holes injected into the magnetic fluid as $r_2 = 1.5$um, the thickness of the gold film covering it as $t_3 = 0.4$ μm, and the depth of the upper polishing depth and the depth of the lower polishing depth as $d_1 = 8.5$ μm and $d_2 = 3.0$ μm, respectively. The upper and lower polishing surfaces were coated with a 0.5 μm gold film ($t_1 = 0.5$ μm, $t_2 = 0.5$ μm). The spacing of adjacent air holes is $c = 6.3$ μm. Data analysis shows light can propagate independently in both cores, thus completing the detection.

We give plots of the dispersion relations of core (1) and core (2) in the X and Y directions, respectively, along with their loss spectra. As shown in Fig. 4, observation of Fig. 4a reveals a clear loss peak in the Y-pol direction and the core mode intersects with the SPP mode out of the resonance wavelength, and there is no loss peak in the X-pol direction. Thus, for the fiber core (1), we mainly study his Y-pol direction. Observing Fig. 4b, c, we can find that the core mode

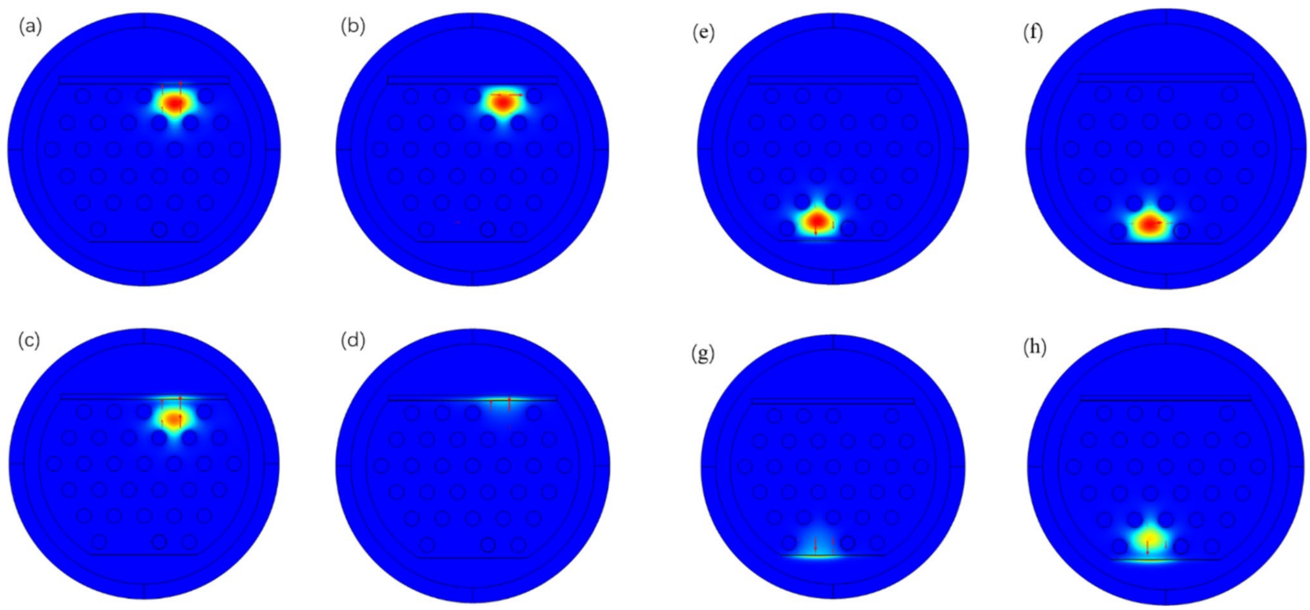

Fig. 3 Electric field distributions of the core 1: **a** Core mode in the direction of Y polarization at 800 nm; **b** core mode in the direction of X polarization at 800 nm; **c** resonance modes in the direction of Y polarization at 892 nm; **d** SPP modes in the direction of Y polarization at 890 nm; Electric field distributions of the core 2: **e** core mode in the direction of Y polarization at 800 nm; **f** resonance modes in the direction of X polarization at 700 nm; **g** SPP modes in the direction of Y polarization at 970 nm; **h** resonance modes in the direction of Y polarization at 970 nm. Arrows indicate polarized direction of electric fields

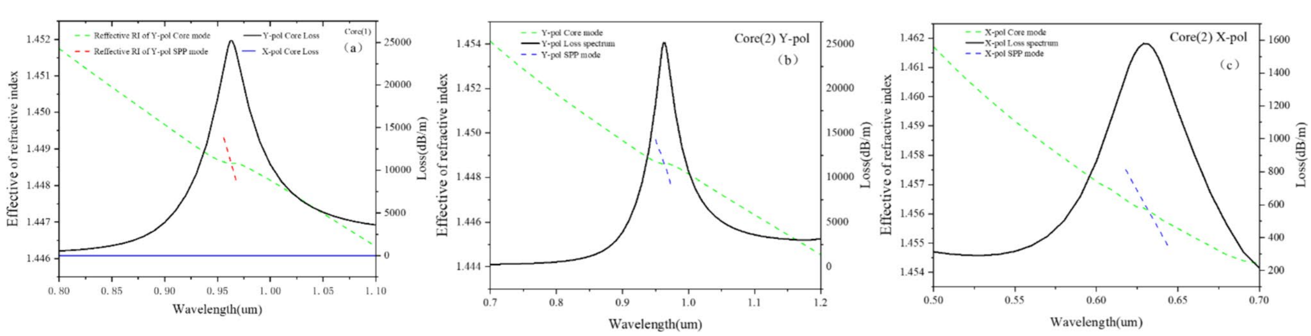

Fig. 4 **a** The dispersion relationship between core mode and SPP mode of core 1, together with the loss spectrum of X-pol and Y-pol.; **b** core 2 Dispersion relation between core mode and SPP modes in Y-pol direction; **c** core 2 Dispersion relation between core mode and SPP modes in X-pol direction

and SPP mode in the X-pol and Y-pol directions are intersected at the resonance wavelength, and there are obvious loss peaks in both directions, so for the core (2), we mainly study his X-pol and Y-pol directions.

Results and Discussion

PML and scattering boundary conditions were introduced in the calculations to improve the accuracy of the results. The designed PCF-SPR sensor was analyzed using the control variable method and the resonance wavelength shift was measured using the wavelength modulation method, which enabled multiparameter measurements. Finally, the sensitivity of the measured parameters is calculated and discussed by data processing.

Refractive Index Sensitivity

Figure 5b shows the fitted curve between the liquid resonance wavelength and RI. The fitting equation in the figure, as well as the data, shows that the fit is good. According to the calculation, the refractive index's sensitivity is up to 20,000 nm/RIU.

Temperature Sensitivity and Magnetic Field Sensitivity

Figure 6b shows the fitted curve between resonance wavelength and temperature. Based on the fitted curve equations as well as the data, it can be seen that the fit is good. The linear sensitivity is calculated to be 5.3 nm/°C because it is needed to derive the linear sensitivity in the subsequent matrix. In addition, the increase in the refractive index leads to the red shift of the phase matching point between the SPW and the core fundamental mode, so the resonance wavelength is red-shifted.

Figures 6 and 7 show that the resonance wavelengths of the magnetic field channel and the temperature channel are blue shifted when the temperature varies. This is due to the negative temperature coefficients of the MF and PDMS for both the magnetic field channel and the temperature channel.

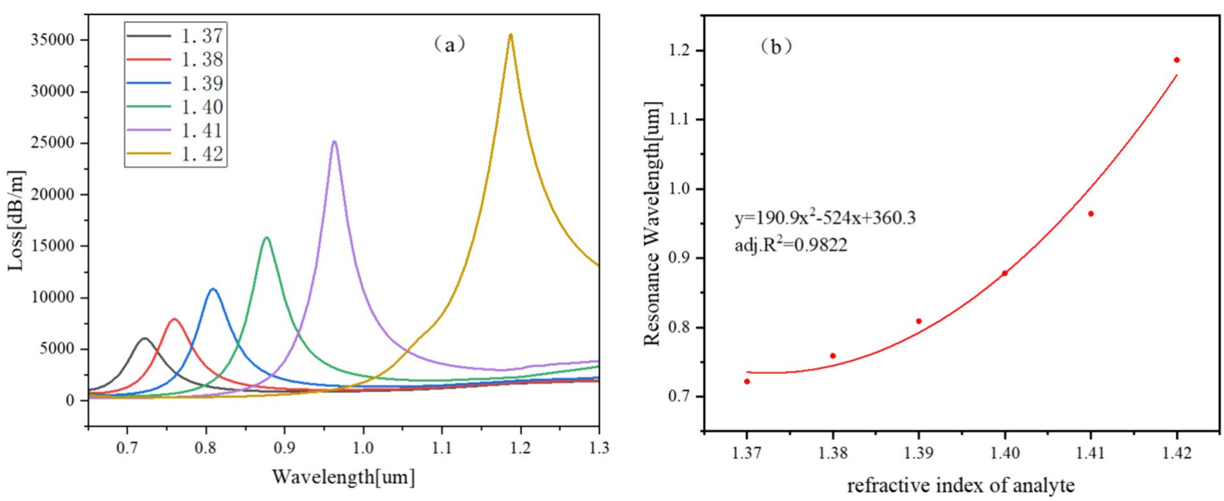

Fig. 5 **a** Variation of the loss spectrum with the refractive index of the liquid and **b** the results of the numerical fitting of the resonance wavelength as a function of the refractive index of the liquid

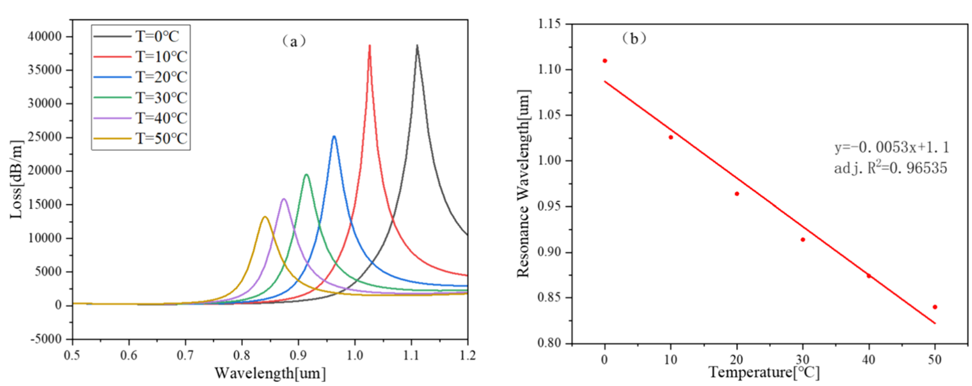

Fig. 6 **a** Variation of loss spectrum with temperature and **b** results of numerical fitting of resonant wavelength as a function of temperature

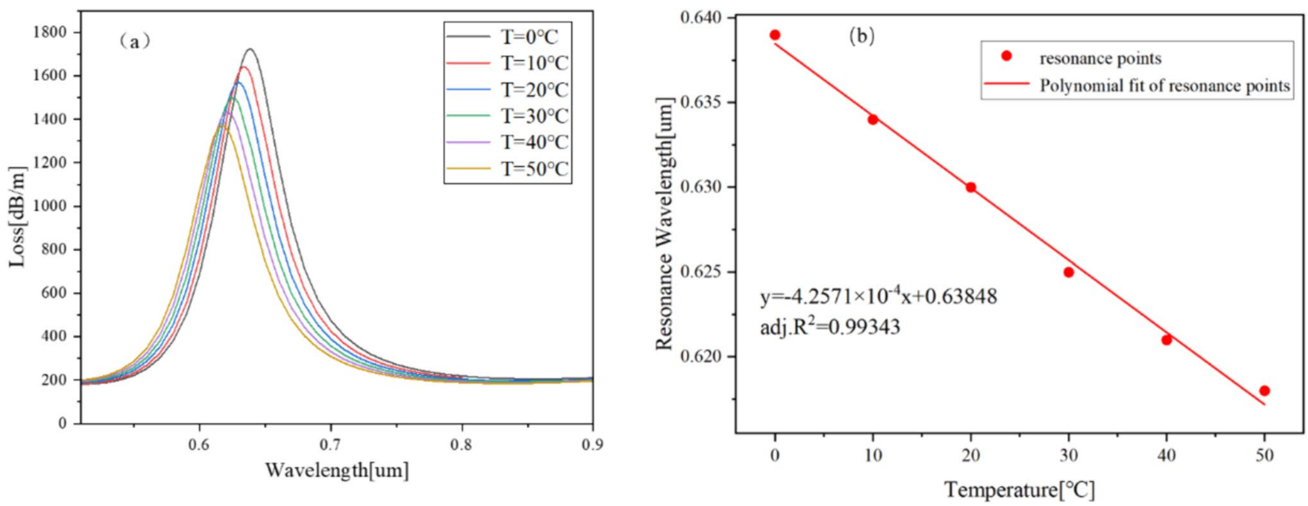

Fig. 7 **a** Loss spectrum of the magnetic field channel as a function of liquid temperature and **b** numerical fitting results of the resonance wavelength as a function of liquid temperature

After linear fitting, the linear sensitivity of the temperature channel was 5300 pm/°C; maximum sensitivity to temperature up to 9200 pm/°C; the sensitivity of the magnetic field channel to temperature was 425.71 pm/°C.

Figure 8 shows that the magnetic field channel resonance wavelengths are red-shifted when the magnetic field strength is varied between 20 and 550 Oe. According to Eq. (4), it can be seen that the magnetic field strength is positively correlated with the MF when the temperature is determined. Therefore, the resonance wavelength is red-shifted, and the linear sensitivity of the magnetic field channel to magnetic field variations is 116 pm/Oe with an R-squared of 0.99214. Moreover, the sensitivity of the temperature channel to magnetic field variations is found to be 0 pm/°C by using Eq. (3).

The linear sensitivity of the temperature channel for temperature and magnetic field changes is 5300 pm/°C and 0 p/°C, respectively. The linear sensitivity of the magnetic field channel for temperature and magnetic field changes is 425.71 pm/Oe and 116 pm/Oe, respectively. According to Eqs. (9) and (10), the temperature and magnetic field sensitivity matrix is as follows:

$$\begin{pmatrix} \Delta T \\ \Delta H \end{pmatrix} = \begin{pmatrix} -0.426 & 0.116 \\ -5.3 & 0 \end{pmatrix}^{-1} \begin{pmatrix} \Delta\lambda_1 \\ \Delta\lambda_2 \end{pmatrix} = \begin{pmatrix} 0 & -0.189 \\ 8.62 & -0.693 \end{pmatrix} \begin{pmatrix} \Delta\lambda_1 \\ \Delta\lambda_2 \end{pmatrix} \tag{10}$$

Since few multi-parameter measurement structures are available, we compare them with some of the two-parameter structures, as shown in Table 1. The table shows that the present design is better than some of the current designs

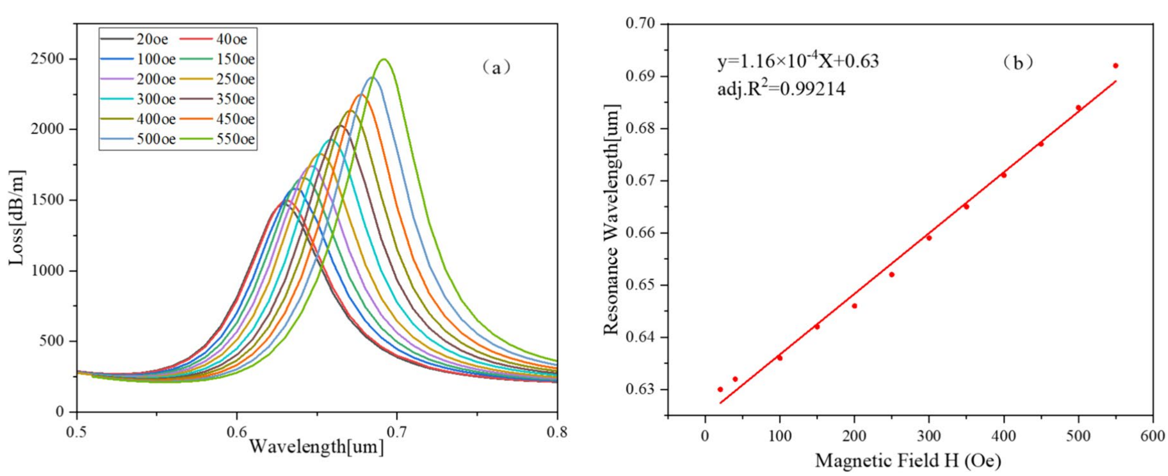

Fig. 8 **a** Variation of loss spectrum with external magnetic field and **b** numerical fitting results of resonant wavelength as a function of magnetic field

Table 1 Comparison of refractive index, temperature, and magnetic field sensitivity with other SPR-based sensor structures

	S(*T*)	*S*(RI)		*S*(*T*)	*S*(RI)		*S*(MF)
Luan et al. [33]	6.18 (nm ℃$^{-1}$)	12,500 (nm/RIU)	Weng et al. [34]	0.14 (nm ℃$^{-1}$)	561.43 (nm/RIU)	Xiao et al. [9]	164 pm/Oe
Yang et al. [35]	1.81 (nm ℃$^{-1}$)	2214.0 (nm/RIU)	Akter et al. [36]	1.00 (nm ℃$^{-1}$)	20,000 (nm/RIU)	Liu et al. [37]	44 pm/Oe
Our	9.2 (nm ℃$^{-1}$)	20,000 (nm/RIU)				Our	116 pm/Oe

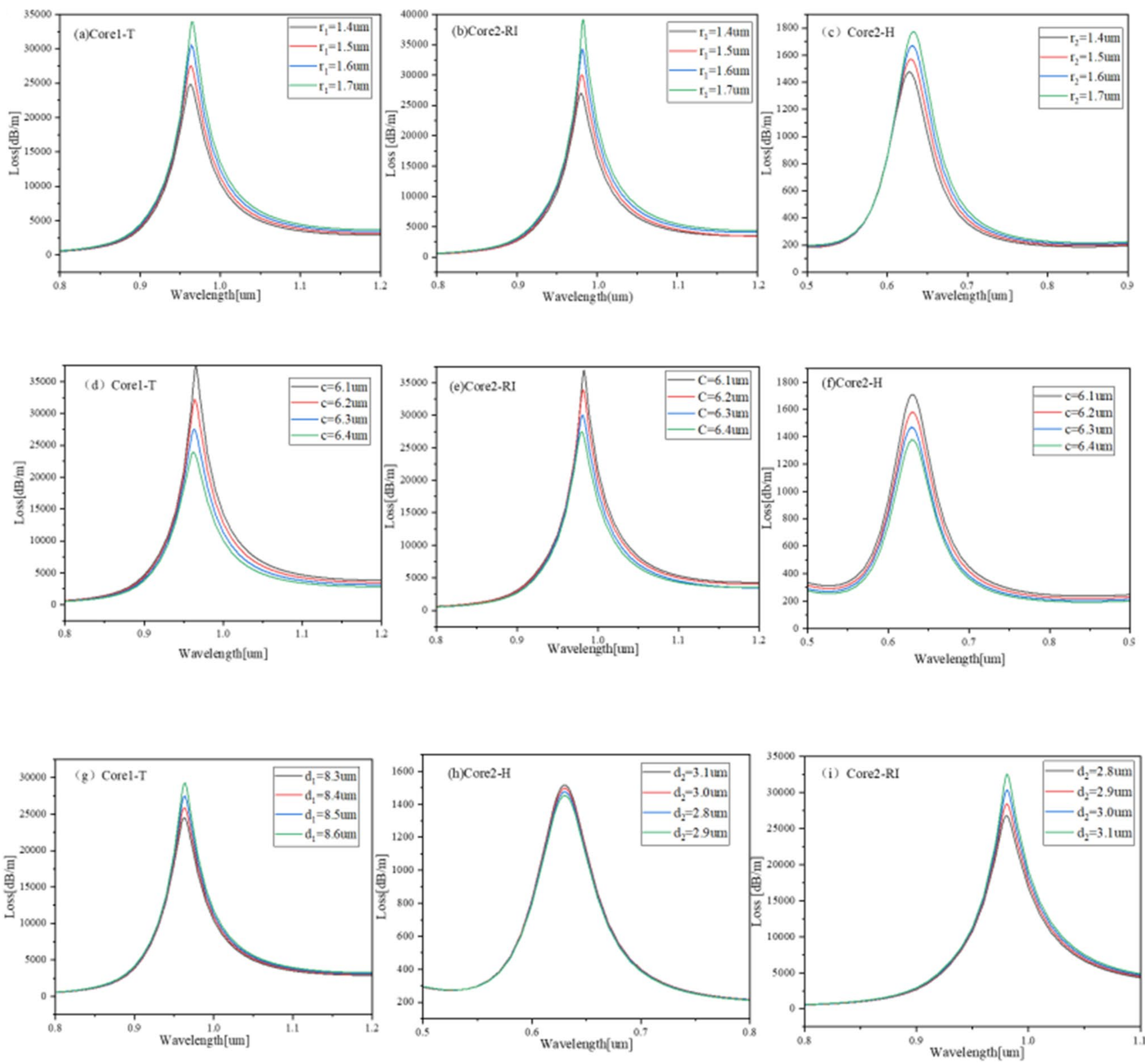

Fig. 9 Loss spectra of the three channels for different values of r_1, r_2, c, d_1 and d_2. **a–c** Loss spectrum of core 1 and core 2 with different values of stomatal radius; **d–f** loss spectrum of core1 and core2 with different values of stomatal spacing; **g–i** loss spectrum of core 1 and core 2 with different values of depths

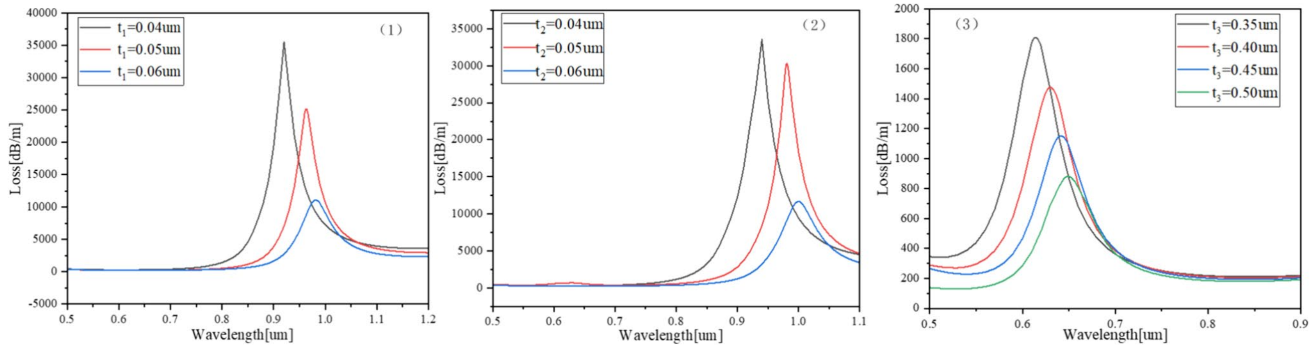

Fig. 10 Loss spectra of temperature channel, refractive index channel and magnetic field channel for different values of t_1, t_2, and t_3. (1) Loss spectra for different gold film thicknesses in the temperature channel; (2) loss spectra corresponding to different gold film thicknesses for the refractive index channel; (3) loss spectra corresponding to different gold film thicknesses for magnetic field channels

of two-parameter structures in terms of temperature and refractive index. The sensitivity of the magnetic field of the present work is also approximately equal to or better than that of other designs.

Influence of Structural Parameters on Sensor Stability

The stability of the designed sensor has a significant impact on its performance. Different structural parameters may have different effects on the sensor performance. In this simulation, different radii of air holes, inter-hole distances and polishing depths are observed to determine whether the sensor is stable. Observations in Fig. 9a–i show that the resonance peaks increase with the increase of the aperture radius under the same environmental conditions. When the aperture radius increases, the fiber core is squeezed horizontally, and more energy leaks into the metal interface, resulting in increased energy loss and an enhanced SPR effect.

Under the same analytical method, an increase in the air hole spacing or polishing depth squeezes the fiber core to some extent, increasing the energy loss and strengthening the SPR effect. However, the resonance wavelength was almost constant, indicating that the sensors involved are relatively stable.

Effect of Gold Film Thickness on Sensing Characteristics

Since the metal film affects the excitation of SPR, we investigated the effect of different polished surface gold films and the thickness of the gold film in the magnetic field channel on the sensor's performance. Figure 10 shows the simulation results. The figure shows that the resonance wavelength position is red-shifted, and the energy loss is gradually reduced with the increase in the thickness of the gold film. This is because less energy can be coupled to the SPW mode with the increase in thickness, resulting in lower losses. The refractive index of the SPW increases as the thickness of the gold film increases. However, the refractive index of the core remains constant, so the matching point between the SPW and the core is red-shifted, and the resonance wavelength position is also red-shifted.

However, when the thickness is chosen, the level of loss and the width of the spectrum will also affect the sensor performance detection. Therefore, by observing the images of temperature and refractive index channels, it was found that the loss was too high for detection at a gold film thickness of 40 nm. In addition, when the gold film thickness is 60 nm, the signal-to-noise ratio is low, which may result in false-positive responses [37, 38]. Finally, the gold film thickness was determined to be 50 nm for the temperature channel. Similarly, using the same analytical method, the gold film thickness was chosen to be 50 nm for the refractive index channel and 45 nm for the magnetic field channel because either the loss was too significant or the spectra were too broad for detection.

Conclusion

This study presents an SPR-PCF sensor that simultaneously measures refractive index, temperature, and ambient magnetic field. Using dual-polished and single-channel filled magnetic fluids makes the deposition of metal films and temperature-sensitive materials easier, thus reducing the difficulty of fabricating the sensor. The relative stability of the designed sensors also reduces their fabrication accuracy. The maximum sensitivity of the RI measurement is 20,000 nm/RIU when the RI of the fluid is 1.36 to 1.42. The sensing matrix is also given when the temperature detection range is 0 °C to 50 °C, and the magnetic field detection range is 20 to 550 Oe. Moreover, calculating the resolution of the refractive index is 4.5×10^{-6}, the resolution of temperature is 2.9×10^{-2}, and the resolution of magnetic field strength is 0.63. The sensor is highly integrated and more miniaturized, providing a new solution for sensor fabrication.

Author Contributions Conceptualization and design of the work: Tianli Huo. Formal analysis and investigation: Tianli Huo, Tianci Gao, and Mingshi Song. Writing of the manuscript: Tianli Huo. Writing—comments and suggestions: Zhiyong Yin and Xili Jing.

Funding This work is supported by the National Natural Science Foundation of China (Grant No. 12074331) and the National Key Research and Development Project (Grant No. 2019YFB2204001).

Data Availability No datasets were generated or analysed during the current study.

Declarations

Ethics Approval Not applicable.

Consent to Participate All authors agree to participate in this investigation.

Consent for Publication All authors agree to participate in this article.

Competing Interests The authors declare no competing interests.

References

1. Hameed MFO, Heikal AM, Younis BM, Abdelrazzak M, Obayya SSA (2015) Ultra-high tunable liquid crystal-plasmonic photonic crystal fiber polarization filter. Opt Express 23(6):7007–7020
2. Homola J, Yee SS, Ggoldglitz G (1999) Surface plasmon resonance sensors: review. Sens Actuators, B Chem 54(1–2):3–15
3. Verma R, Srivastava SK, Gupta BD (2012) Surface-plasmon-resonance-based fiber-optic sensor for the detection of low-density lipoprotein. IEEE Sens J 12(12):3460–3466
4. Wang G, Li S, An G, Wang X, Zhao Y, Zhang W et al (2016) Highly sensitive d-shaped photonic crystal fiber biological sensors based on surface plasmon resonance. Opt Quant Electron 48(1):1–9
5. Bilal MM, Bi W, Liu X, Yang L, Wa J, Madni HA (2019) Magnetic field sensor based on the magnetic fluid infiltration into the cladding air holes of the solid-core photonic crystal fiber. Opt Eng 58(9):096107
6. Bilal MM, Lopez-Aguayo S, Thottoli A (2023) Numerical analysis of solid-core photonic crystal fiber based on plasmonic materials for analyte refractive index sensing. Photonics 10(10):1070
7. Hassani A, Skorobogatiy M (2006) Design of the microstructured optical fiber-based surface plasmon resonance sensors with enhanced microfluidics. Opt Express 14(24):11616–11621
8. Tian M, Lu P, Chen L, Lv C, Liu D (2012) All-solid d-shaped photonic fiber sensor based on surface plasmon resonance. Opt Commun 285(6):1550–1554
9. Xiao G, Ou Z, Yang H, Xu Y, Li J (2021) An integrated detection based on a multi-parameter plasmonic optical fiber sensor. Sensors 21(3):803
10. Yin Z, Jing X, Feng Y, Gao Z, Wu B, Wang C (2022) Refractive index and temperature dual parameter sensor based on a twin-core photonic crystal fiber. J Phys D Appl Phys 55(15):155108
11. Pagnoux D, Fevrier S, Leproux P, Huy MCP, Pryamikov A, Viale P et al (2005) Microstructured fibers for sensing applications (Invited Paper). 17thInternational Conf. on Optical Fibre Sensors Proc. SPIE Int Soc Opt Eng 5855:5–8
12. Yi C, Zhang P, Chen F, Dai S, Wang X, Xu T et al (2014) Fabrication and characterization of ge20sb15s65 chalcogenide glass for photonic crystal fibers. Appl Phys B 116(3):653–658
13. El Hamzaoui H, Ouerdane Y, Bigot L, Bouwmans G, Capoen B, Boukenter A et al (2012) Sol-gel derived ionic copper-doped microstructured optical fiber: a potential selective ultraviolet radiation dosimeter. Opt Express 20(28):29751–29760
14. Russel PSJ, Birks TA, Knight JC, Mangan BJ (2006) Photonic crystal fibers. Lightwave Technol 24:4729–4749
15. Kiang KM, Frampton K, Monro TM, Moore R, Tucknott J, Hewak DW et al (2002) Extruded singlemode non-silica glass holey optical fibres. Electron Lett 38(12):546–547
16. Kanth Kumar VVR, George AK, Reeves WH, Knight JC, Russell PSJ, Omenetto FG et al (2002) Extruded soft glass photonic crystal fiber for ultrabroad supercontinuum generation. Opt Express 10
17. Hasegawa T (2012) Design and fabrication of bismith-silicate photonic crystal fiber. Opt Commun 285(19):3939–3944
18. Qingli X, Yuzhi C, Xuejin L, Zhen Y, Lele W, Youfu G et al (2017) Characteristics of d-shaped photonic crystal fiber surface plasmon resonance sensors with different side-polished lengths. Appl Opt 56(5):1550
19. Chen Y, Xie Q, Li X, Zhou H, Hong X, Geng Y (2017) Experimental realization of d-shaped photonic crystal fiber spr sensor. J Phys D Appl Phys 50(2):025101
20. Bhattacharyya D, Senecal K, Marek P, Senecal A, Gleason KK (2011) High surface area flexible chemiresistive biosensor by oxidative chemical vapor deposition. Adv Func Mater 21(22):4328–4337
21. Wong WC, Chan CC, Boo JL, Teo ZY, Tou ZQ, Yang HB et al (2013) Photonic crystal fiber surface plasmon resonance biosensor based on protein g immobilization. IEEE J Sel Top Quantum Electron 19(3):4602107–4602107
22. Li B, Yan X, Zhang X, Wang F, Li S, Suzuki T et al (2021) No-core optical fiber sensor based on surface plasmon resonance for glucose solution concentration and temperature measurement. Opt Express 29:12930–12940
23. Akowuah EK, Gorman T, Ademgil H, Haxha S, Robinson GK, Oliver JV (2012) Numerical analysis of a photonic crystal fiber for biosensing applications. IEEE J Quantum Electron 48(11):1403–1410
24. Wu JJ, Li SG, Liu Q, Shi M (2017) Photonic crystal fiber polarization filter with two large apertures coated with gold layers. Chin Phys B 26:114209
25. Zongda Z, Lu L, Zhihai L, Yu Z, Yaxun Z (2017) Surface-plasmon-resonance-based optical-fiber temperature sensor with high sensitivity and high figure of merit. Opt Lett 42(15):2948
26. Yang SY, Chieh JJ, Horng HE et al (2004) Origin and applications of magnetically tunable refractive index of magnetic fluid films. Appl Phys Lett 84(25):5204–5206
27. Yuan C, Lou Z, Wang W, Yang L, Li Y (2019) Synthesis of fe3c@c from pyrolysis of fe3o4-lignin clusters and its application for quick and sensitive detection of prpsc through a sandwich spr detection assay. Int J Mol Sci 20(3)
28. Lou Z, Han H, Zhou M, Wan J, Sun Q, Zhou X et al (2017) Fabrication of magnetic conjugation clusters via intermolecular assembling for ultrasensitive surface plasmon resonance (spr) detection in wide-range concentration. Anal Chem 89(24):13472
29. Hong CY, Horng HE, Yang SY (2010) Tunable refractive index of magnetic fluids and its applications. Phys Status Solidi 1(7):1604–1609

30. Yong Z, Yuyan Z, Di, & Wu, et al (2013) Magnetic field and temperature measurements with a magnetic fluid-filled photonic crystal fiber bragg grating. Instrum Sci Technol 41(5):463–472
31. Fu H, Zhang M, Ding J, Wu J, Zhu Y, Li H et al (2019) A high sensitivity d-type surface plasmon resonance optical fiber refractive index sensor with graphene coated silver nano-columns. Opt Fiber Technol 48(2):34–39
32. Bilal MM, López-Aguayo S, Szczerska M, Madni HA (2022) Multi-functional sensor based on photonic crystal fiber using plasmonic material and magnetic fluid. Appl Opt 61:10400–10407
33. Luan N, Ding C, Yao J (2016) A refractive index and temperature sensor based on surface plasmon resonance in an exposed-core microstructured optical fiber. IEEE Photonics J 8(2):4801608
34. Weng S, Pei L, Liu C, Wang J, Li J, Ning T (2016) Double-side polished fiber spr sensor for simultaneous temperature and refractive index measurement. IEEE Photonics Technol Lett 28(18):1916–1919
35. Yang XC, Lu Y, Liu BL, Yao JQ (2017) Simultaneous measurement of refractive index and temperature based on spr in d-shaped mof. Appl Opt 56:4369–4374
36. Akter S, Ahmed K, El-Naggar SA, Taya SA, Nguyen TK, Dhasarathan V (2020) Highly sensitive refractive index sensor for temperature and salinity measurement of seawater. Optik 216:164901
37. Hai L, Cancan C, Haoran W, Wen Z (2020) Simultaneous measurement of magnetic field and temperature based on surface plasmon resonance in twin-core photonic crystal fiber. Optik 203:164007
38. Rifat AA, Ahmed R, Mahdiraji GA, Adikan FRM (2017) Highly sensitive d-shaped photonic crystal fiber based plasmonic biosensor in visible to near-ir. IEEE Sens J 17:2776–2783